A Method for Substrate Permittivity and Dielectric Loss Characterization Up to Subterahertz Frequencies

Patrick Seiler, *Graduate Student Member, IEEE*, and Dirk Plettemeier, *Member, IEEE*

***Abstract*— In this paper, a method for substrate permittivity and loss tangent characterization applicable for frequencies in the subterahertz range is presented. Planar transmission lines fabricated on three different printed circuit board (PCB) materials and four different on-chip/on-wafer materials are being used for measurement along with a wafer probing station equipped with on-wafer probes and frequency extenders. A comprehensive procedure for calculation of substrate permittivity, total loss, characteristic impedance, and dielectric loss tangent is presented. Measurement data up to 67 GHz is given in case of PCB and up to 500 GHz in case of on-chip/on-wafer materials and compared against reference data and competitive materials from recent publications.**

***Index Terms*— Dielectric measurement, materials testing, permittivity, submillimeter-wave measurements, transmission-line (TL) measurements.**

I. Introduction

With increasing frequency up to the subterahertz/submillimeter-wave range and the desire to optimize performance of related applications, precise knowledge of the permittivity and dielectric loss of a substrate being used in a planar application is crucial: high performance of the desired application can often be achieved only by using specific values for the material properties during the design process of the application. In particular, the integration of planar devices for very broadband applications at high frequencies often demands low-dielectric-constant dielectrics with low dispersion and loss, assuring a predictable performance over the broad frequency range [1].

Often, specially designed back-end-of-line (BEOL) processes are used on top of commonly used wafer materials to provide an integration platform with good high-frequency characteristics. Usually, the materials used in BEOL processes are only specified at discrete frequencies often in the megahertz range or not specified at all.

Therefore, material characterization at these frequencies is of interest to the developing community, although not a lot of characterization techniques suitable in terms of frequency range and measurement setup exist: resonant methods inherently offer the highest accuracy due to the high-quality factors of the resonators being used, enabling a precise determination of the material parameters of a sample placed, e.g., within a cavity, especially for low-loss materials [2], [3]. Their applicability, however, is limited to single resonant frequencies of one or more (higher) modes excited within the resonator, thus offering only discrete measurements and requiring higher mode identification [4]–[6]. Some methods use models specifically tailored for a certain application [7], [8], while others add the requirement of extensive numerical calculations [9], [10]. In either case, often a specialized measurement cell and sample size is required, which becomes very cumbersome to fabricate and handle due to the small dimensions at these frequencies, effectively rendering these methods not suitable for application with increasing frequency or in the subterahertz range. Most nonresonant methods are broadband transmission/reflection methods [11]–[13], but usually offer less accuracy due to the lower quality factors of the measurement systems being used. Regardless of whether a specialized measurement cell is required or not, methods based on coaxial [11], [13], [14] or waveguide [12], [13], [15] technology are inherently limited in their applicability in the subterahertz range: coaxial technology is merely available up to 110 GHz. Multiple waveguides are required for broadband measurements, as each one only covers its operating frequency range. In both cases, most methods require the sample to at least partially fit [16] the cross section of the coaxial (110 GHz: 1.0 mm inner diameter) or waveguide structure (WR-03, 220–325 GHz: 0.86×0.43 mm^2), which imposes the same restrictions concerning sample fabrication and handling as discussed earlier for the resonant case. Again, some methods use models specifically tailored for a certain application [17], add the requirement of numerical calculations or are sensitive to errors such as connector repeatability [18] or impedance mismatch [19]. Nonresonant time-domain methods such as the short-pulse propagation method originally proposed in [20] require very fast source excitations, as bandwidths up to the subterahertz-range translate to pulse widths in the

Manuscript received January 30, 2018; revised July 27, 2018; accepted December 9, 2018. Date of publication March 19, 2019; date of current version April 3, 2019. This work was supported by the German Research Foundation (Deutsche Forschungsgemeinschaft) through the Collaborative Research Center under Grant SFB 912-HAEC. *(Corresponding author: Patrick Seiler.)*

The authors are with the Chair for Radio Frequency and Photonics Engineering, Technische Universität Dresden, 01062 Dresden, Germany (e-mail: patrick.seiler@tu-dresden.de).

Color versions of one or more of the figures in this paper are available online at http:ieeexplore.ieee.org.

Digital Object Identifier 10.1109/TMTT.2019.2897102

single-digit picosecond range. Since broadband receivers are an additional requirement, the signal-to-noise ratio is lower than for a measurement in the frequency domain using a network analyzer (NA) [21]. Both the source excitations as well as receivers are not readily available in the electrical domain. These limitations do not apply to frequency-domain measurements using an NA, as frequency extenders up to at least 500 GHz are commercially available and the standard equipment for measurement at these frequencies in most laboratories measuring in the subterahertz-range today [22].

As originally proposed for transmission lines (TLs) in [11] and [12], a transmission/reflection method enables broadband permittivity characterization from dc onward. It can be used in conjunction with planar TLs: S-parameters obtained from the measurement can be used to extract the effective propagation characteristics such as the effective permittivity of TLs on printed circuit board (PCB) [23] as well as on-chip/on-wafer substrates [24]. Since the suggested approach does not cover the effects related to internal inductance and roughness of the TLs [25], respective corrections need to be applied to obtain the correct value for the effective permittivity. In this paper, the comprehensive theory for the proposed approach is given along with the extensions covering the derivation of the permittivity, the correction for inductance-related effects and the determination of the dielectric loss. A continuous fit obtained by simulations with Ansys EM Suite is used to map the corrected effective permittivity to the substrate permittivity. Since the total loss can be determined directly from the measurement, but a separation or direct calculation of the dielectric loss is not possible, an alternative approach using the Kramers–Kronig relations is presented, which gives the option of fitting the measurement data to the presented model as well. New measurement data on common BEOL materials up to 500 GHz backs the feasibility in the subterahertz frequency range. Since the reference data on the material properties of BEOL materials is usually insufficient or not available at all at these frequencies, new measurement data on three different PCB materials is given to discuss the presented approach and compare the results to available reference data given by the PCB manufacturer, showing the general feasibility of the presented method.

Since TLs are inherently broadband and the upper frequency limit is only subject to the fabrication process (i.e., minimum planar dimensions of TLs and height of substrate), the proposed method outperforms the aforementioned techniques using resonators or other frequency-limited measurement cells in terms of frequency coverage. As only a measurement of S-parameters of TLs on a substrate is required, no further development of a specialized measurement cell or micromachining and handling a sample of small size is necessary, as the sample is the substrate. The measurement is taken in the frequency domain using an NA, which offers higher signal-to-noise ratio compared to measurements in the time-domain. Since a multiline thru-reflect-line (mTRL) calibration and precisely placeable on-wafer probes are used, impedance mismatch, as well as connector reproducibility, is no issue. The applied theory consists only of general wave propagation and TL theory, and does not require any specialized model or specifically tailored equations. The method itself can be implemented easily using a programming framework of the reader's choice (the authors used MATLAB R2016a for implementation) and does not need extensive computational effort. In fact, the authors intend this paper to serve as a basis for other laboratories performing subterahertz or corresponding measurements: integrating the suggested procedure into their measurement setups should easily enable the related substrate material characterization. Only the measurement equipment to enable subterahertz measurements, which is most likely available at these laboratories anyway, is necessary. To the best of the author's knowledge, no such documentation giving a comprehensive approach to this topic exists so far.

This paper is structured as follows. In Section II, the measurement setup is presented, including calibration and design considerations concerning the TLs. An overview of the measurement approach is given, introducing the general procedure consisting of measurement and application of the theory in a step-by-step way. The theory presented in Section III follows the same structure and gives details on the single steps in respective sections. Parts of the theory presented in this paper have already been published in conference by Seiler *et al.* [23]–[25], but are extended in this paper. The measurement results and discussion thereof is given in Section IV, followed by a conclusion of this paper in Section V.

II. Measurement Setup and Procedure

A. Choice of Materials

To show the general feasibility of the proposed procedure, TLs on different substrate materials are fabricated for measurement.

1) PCB.
   a) Rogers Ultralam 3850 (RO3850, Rogers Corporation).
   b) Rogers 3006 (RO3006, Rogers Corporation).
   c) Rogers 3010 (RO3010, Rogers Corporation).
2) On-chip/on-wafer.
   a) Polyimide (PI, HighTec MC AG).
   b) Ormocer (ORMO, Fraunhofer Gesellschaft).
   c) Benzocyclobutene (BCB, Dow Chemical Company).
   d) Silicon dioxide (SiO_2, IHP-GmbH).

Details on the specific materials and the fabrication processes used can be found at the above-mentioned manufacturers for each substrate material. On the three PCBs, both microstrip (MS) and grounded coplanar waveguide (GCPW) TLs are fabricated. On the PI, ORMO, and BCB substrates, MS TLs are fabricated. The on-chip substrates are layered on either a silicon or ceramics wafer as mechanical support, which is isolated from the thin substrate under test by a ground metal layer. On the SiO_2, coplanar waveguide (CPW) TLs are fabricated, as MS TLs are not feasible due to the constraints of the fabrication process. The CPW TLs are embedded within the SiO_2 that is layered on top of a silicon wafer: the silicon wafer with a height of 300 μm is covered with 10.83 μm SiO_2, which supports the metallization layer of thickness 3.0 μm forming the CPW structure. An additional SiO_2 layer with

TABLE I
MEASURED VALUES OF TL GEOMETRIES

	height [μm]	width [μm]	thickness [μm]	gap [μm]
RO3850	100	235	23	101
RO3060	130	178	17	97
RO3010	130	90	33	120
PI	20	47	5.2	n/a
ORMO	11	23	3	n/a
BCB	10	23	2	n/a
SiO_2	10.83	2.4	3.0	4.0

a height of 1.5 μm on top of the metallization is used for passivation of the surface. Since SiO_2 constitutes the substrate around the CPW, and the distance to the silicon wafer is more than three times higher than the CPW thickness, the resistivity of the silicon wafer can be neglected.

The PCB substrates are only measured up to 67 GHz and will serve as proof-of-principle measurements. For these substrates, the manufacturer gives measurement data for the permittivity and loss tangent. Since such data are usually not available for the on-chip materials listed above, and especially for the high bandwidth measured in this paper, no validation of the presented method by comparison with reference data would be possible otherwise.

Using simulations with Ansys EM Suite and an estimation for the substrate permittivity for each substrate, the geometries for the TLs on all substrates, except for SiO_2, are chosen to 50 Ω over the measurement frequency range, while the TLs on SiO_2 are chosen to about 30 Ω. However, due to the usual process deviations for the commercial PCB as well as the custom on-chip processes used, slight deviations to the target geometry are unavoidable. The final 2-D geometries, as well as the fabricated layer buildup of the TLs, are measured using both a conventional lab microscope with high resolution as well as raster electron microscopy (especially for the layer buildup in case of the on-chip materials). The final values for the TLs on the substrates are given in Table I. The values in the rightmost column ("gap") represent the distance of signal and ground conductor in case of GCPW (for the PCB substrates) and CPW (for the SiO_2 substrate). Since any deviation from the design values to the fabricated ones is covered by the microscopic analysis and considered in the simulation later on, the fabrication uncertainty is irrelevant for the method presented in this paper.

B. Measurement Setup

For the actual measurement of the S-parameters, a wafer probing station with GGB Picoprobes built in a ground-signal-ground fashion is used. On-wafer probes are the usual choice of connectors establishing an interface with a planar substrate for measurement of frequencies in the subterahertz range. This is not to be understood as a restriction, since the method presented in this paper can be used with any suitable connector for the frequency range of interest, i.e., commercially available coax connectors for measurements up to 67 GHz. To enable a broadband measurement, the NA is equipped with frequency extenders for the additional ranges 140–220, 220–325, and 325–500 GHz, thus allowing measurements from 500 MHz to 500 GHz,[1] see Fig. 1 for the measurement setup. Consequently, a different set of probes is used for each frequency band as well.

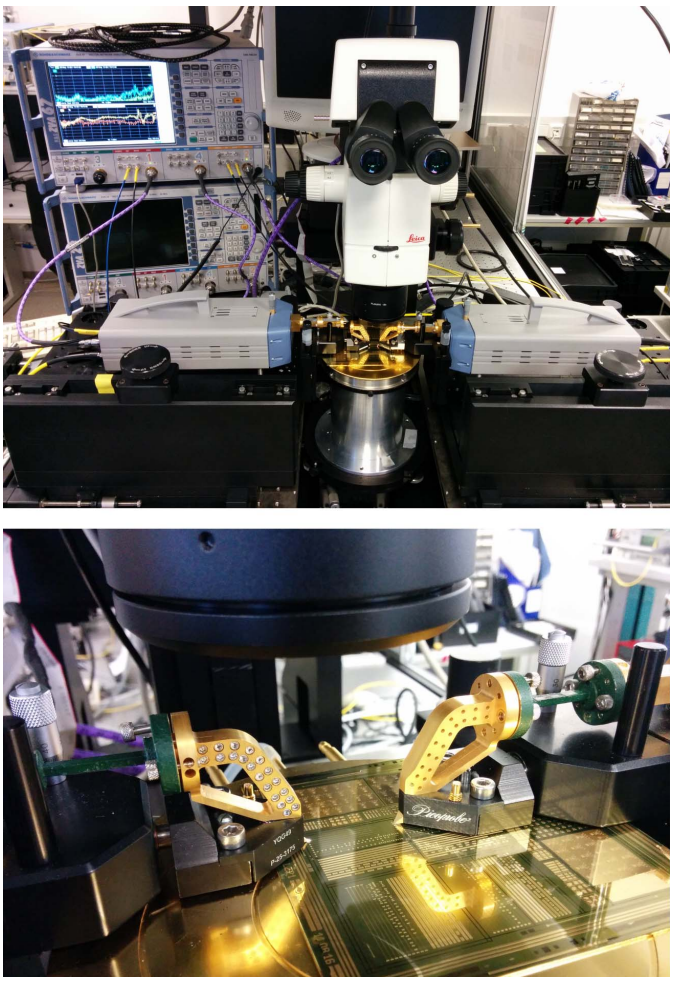

Fig. 1. Overview (top) and detailed view (bottom) on the wafer probing station showing PI substrate contacted by on-wafer probes. Straight waveguides on the sides connect the probes to frequency extenders, which extend the measurement range of the NA to 500 GHz. Different sets of TL layouts that have been tested can be seen on the substrate. A high-resolution microscope as seen on the top is used to control precise probe placement. The frequency extenders are connected to the NA and placed on translation stages, allowing controlled movement of the probes.

C. Calibration

Prior to measurement, a custom mTRL calibration is done [26]. To avoid calibration performance decrease or mismatch of any kind (i.e., due to an off-chip calibration substrate showing a different TL layout or substrate permittivity), custom mTRL standards are included on each substrate. The thru and lines show an identical TL and probe pad structure, and only differ in length, whereas the reflect is designed as a block of vias at the end of a TL resembling one half of the designed thru. To properly cover the broad measurement frequency range, a number of lines is implemented for calibration on

[1] Due to the lack of frequency extenders for 90–140 GHz in our laboratory, the measurement data shows a frequency gap from 67–140 GHz.

TABLE II
CUSTOM MTRL LINE STANDARDS

	RO3850 [μm]	PI [μm]	ORMO [μm]
line 1	1120	150	161
line 2	1818	199	194
line 3	4818	397	242
line 4	7709	1192	302
line 5	19271	4730	1210
line 6	n/a	18737	4838
line 7	n/a	n/a	19352

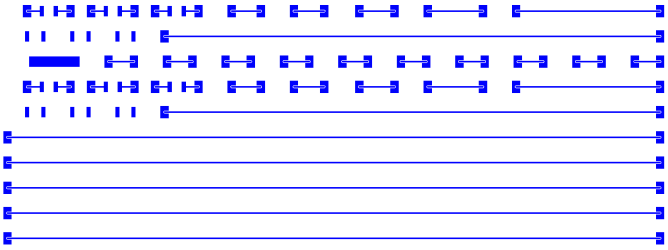

Fig. 2. Layout on PI consisting of custom calibration standards at the top as well as the five TLs for measurement at the bottom. The calibration standards have been included multiple times to allow some redundancy and counter wearing off of the probe pads due to measurement. The overall size of the layout shown here is about 26.3 × 9.5 mm^2, mainly due to the TLs for measurement.

each substrate, see Table II for the chosen lines on three of the measured substrates. Considering the different number of lines for each substrate, most of the custom calibration standards have originally been designed for different applications, which were not necessarily intended to work up to 500 GHz. In case of the PI and ORMO substrates, a higher number of lines than necessary is included in the layout on purpose, to increase the number of (virtual) lines with overlapping operational frequency ranges for the mTRL calibration. For determination of the line lengths prior to fabrication, an estimate of the substrate permittivity for each substrate is used.

Since a strong deviation of the estimated permittivity during design would change the line bandwidths quite a lot, sufficient bandwidth overlap of each line is included to account for errors of such kind. For further details and guidelines on choosing mTRL calibration standards, the authors refer to [26].

D. Layout and Probe Pad Design

Besides the set of calibration standards, five TLs of length 25 mm are included on every layout for measurement, except for the one on SiO_2, due to the limited chip space. An overview on the layout on PI including two sets of custom calibration standards as well as the five measurement TLs is given in Fig. 2. Since the on-wafer probes used for measurement are built in a ground–signal–ground fashion, the probe pad is designed as a GCPW structure showing an impedance of about 50 Ω and, thus, matching the MS TL following the pad structure. A precise probe placement is critical as it influences the measured electrical length of the TL, which is why the launch of the TL is designed in a semicircular fashion (see Fig. 3). This eases probe placement under the microscope, as the transition from the semicircle at launch

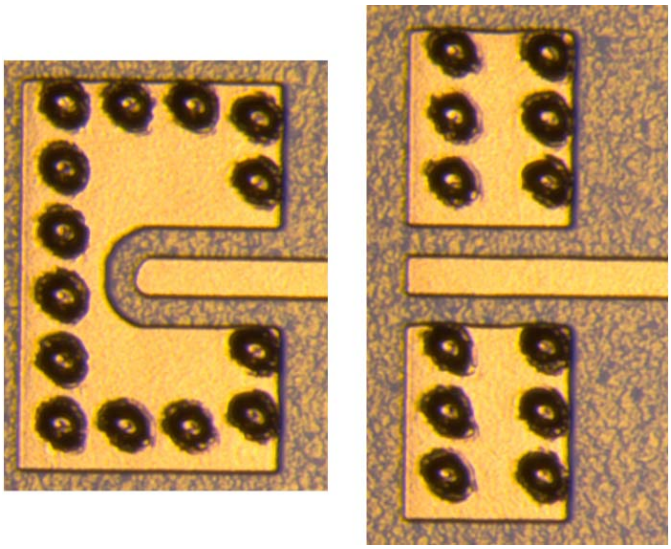

Fig. 3. Photographs of two different realized probe pad structures on PI. The transition from the semicircle at launch to the actual straight section of the TL (left) can be targeted conveniently with the probe tips during placement compared to the straight layout (right). In both cases, the MS width is 47 μm.

to the actual straight section of the TL can be targeted conveniently with the probe tips during placement compared to a probe pad built in a straight fashion, where no such orientation is given. In addition, this kind of layout alteration is easily implemented during the design and eases the probe placement without disturbing the actual probe pad interface. Even though both structures have been realized, only the measurement data for the semicircular pad structure suggested above is given in this paper. The specific pad layout and size is a major limiting factor in terms of maximum measurement frequency, especially considering the probe pad on PCBs and the restrictions of the commercially available processes, such as minimum linewidth, line gap, and the necessary sizes of via pads for ground connection. As a conclusion to this problem and from the experience of the authors, the probe pad itself should always have a minimum size in both planar directions and only show enough metallic surface to cover the probe tips, so that excitation of higher modes or probe pad resonances are conveniently suppressed. In addition, vias required should be placed close to the probe tips and edge of the metal surface, and therefore, shortening any edge of the pad that could possibly serve as a radiating element. Due to the aforementioned reasons and the commonly available heights of PCB substrates, measurements higher than at best 100 GHz are usually not feasible on PCB: Even PCB manufactured especially for RF purposes are usually not offered with a height lower than 50 μm, and most PCB processes demand minimum planar dimensions of at least 75 μm. In addition, conventionally drilled vias are hardly smaller than 150 μm in diameter and usually demand pad sizes of double that diameter for fabrication. On-chip substrates with higher resolution in planar fabrication, a buildup consisting of very thin layers and very small (etched or lasered) vias are not bound to this limitation. A more detailed analysis of this issue has been given by Seiler *et al.* [27].

E. Measurement and Characterization Procedure

First, an appropriate planar calibration is applied, which deembeds the probes as well as the pad structure from further measurement by shifting the reference plane onward the TL. As described in the previous section, an mTRL calibration using custom standards is used in this paper.

Second, the propagation constant needs to be extracted from the measurement. For this, the S-parameters of a TL (i.e., the five lines implemented for measurement) are measured after calibration and the propagation constant can be extracted using the approach given in Section III-A. This approach using TLs for measurement after calibration does only require the NA to supply the operator with an appropriate calibration algorithm as described before. In principle, no custom calibration standards as used in this paper would be necessary for this approach, since the calibration could be done beforehand applying any available calibration routine fulfilling the requirements as described earlier. However, if there is a custom implementation of mTRL or any other routine already giving an estimate for the propagation constant after calibration available at the laboratory, this estimate can be used for the following steps as well, as is done in this paper.

Third, by applying the equations given in Section III-B, the effective permittivity can be calculated from the propagation constant.

Fourth, the TL's characteristic impedance can be extracted and used for calculation of the related RLGC-parameters as well as a correction of internal inductance and roughness-related effects, which is further explained in Section III-C and Section III-D.

Fifth, using the effective permittivity obtained by measurement and simulations done with Ansys EM Suite, the substrate permittivity can be determined. A simple sweep for the given TL geometry allows for extraction of the effective permittivity for any given substrate permittivity, as discussed in Section III-E.

Sixth, the total loss can be determined from the extracted propagation constant. To ensure a good determination of the loss, the rather high length of 25 mm is chosen for the TLs used for measurement, so that the propagating signal can accumulate some loss while traveling along the TL even on a low loss substrate. Besides the total loss, especially the dielectric loss bound to the TL substrate is of interest. The loss measurement, limitations thereof, and a method for calculation of the associated dielectric loss tangent is discussed in Section III-F.

III. Theory

A. Extraction of Propagation Constant From S-Parameters

Using signal flow graph theory, useful relations between S-parameters and transmission (T) as well as reflection (Γ) coefficient can be found [11]

$$S_{11} = S_{22} = \frac{(1 - T^2)\Gamma}{1 - \Gamma^2 T^2} \tag{1a}$$

$$S_{21} = S_{12} = \frac{(1 - \Gamma^2)T}{1 - \Gamma^2 T^2}. \tag{1b}$$

Combining (1a) and (1b), the coefficients can be expressed by the S-parameters

$$T = \frac{(S_{11} + S_{21}) - \Gamma}{1 - (S_{11} + S_{21})\Gamma} \tag{2a}$$

$$\Gamma = K \pm \sqrt{K^2 - 1} \tag{2b}$$

$$K = \frac{S_{11}^2 - S_{21}^2 + 1}{2S_{11}} \tag{2c}$$

where the sign in (2b) is chosen so that $|\Gamma| \leq 1$, which is required for causal, passive materials.

Since a single transverse electromagnetic (TEM) mode of propagation in a TL is being assumed, the transmission coefficient is given by

$$T = e^{-\gamma l} \tag{3}$$

where l is the length of the TL. The propagation constant can be calculated from (3) in a direct manner

$$\gamma = -\frac{\ln(T)}{l} = -\frac{1}{l}\Big[\ln(|T|) + j[\varphi(T) + 2\pi n]\Big] \tag{4}$$

where $n \in \mathbb{Z}$, φ denotes the phase, and j stands for the imaginary unit. Due to the ambiguous nature of the complex logarithm, (4) becomes a multivalued problem. The resulting phase ambiguity can easily be solved using phase unwrapping and offset correction of the phase to ensure causality (i.e., $\varphi = 0$ for angular frequency $\omega = 0$).

The given transmission coefficient as well as the following theory assumes a single TEM wave propagating through media with a homogeneous cross section. This cannot be satisfied in a straight manner by a planar TL such as MS, since the cross section is formed by the dielectric substrate below the TL as well as an air section above the TL. However, most lines of that kind can be assumed to work in a quasi-TEM mode[2] with effective material parameters modeling a homogeneous cross section, as long as a single mode of operation is maintained and higher order modes are sufficiently suppressed. Design rules and a review on how to avoid higher order modes in planar TLs such as MS or GCPW have been given by Seiler *et al.* [23].

B. Derivation of Permittivity From Propagation Constant

Considering a (quasi-)TEM wave propagating through a homogeneous, nonmagnetic material (relative permeability $\mu_r = 1$), the propagation constant is given as

$$\gamma = j\frac{\omega}{c} = j\omega\sqrt{\mu_0\varepsilon} = j\omega\sqrt{\mu_0\varepsilon_0\varepsilon_r'(1 - j\tan\delta)} \tag{5}$$

where c is the velocity of light inside the material, and μ_0 and ε_0 are the vacuum permeability and permittivity, respectively. The complex permittivity is given by

$$\varepsilon = \varepsilon' - j\varepsilon'' = \varepsilon_0\varepsilon_r = \varepsilon_0(\varepsilon_r' - j\varepsilon_r'') \tag{6}$$

[2]Field components in longitudinal direction are existent, but are negligible in comparison to the transverse components. This assumption is valid for the MS TL measured within this paper, since even the largest MS width of 47 μm is roughly ten times smaller than the effective wavelength at the maximum measurement frequency of 500 GHz.

where ε_r stands for the relative permittivity of the material. The primed and double-primed characters denote the real and imaginary parts of the related quantity. The effective loss tangent is defined as

$$\tan\delta = \frac{\sigma_c}{\omega\varepsilon'} + \frac{\varepsilon''}{\varepsilon'} = \tan\delta_c + \tan\delta_d. \tag{7}$$

By using this formulation, loss due to electric conductivity σ_c can be distinguished from dielectric loss related to $\tan\delta_d = (\varepsilon''/\varepsilon')$.

Since the propagation constant is a complex quantity consisting of a loss constant α and a phase constant β, it can also be written as

$$\gamma = \alpha + j\beta. \tag{8}$$

By squaring the propagation constant and separating it into real and imaginary part

$$\mathrm{Re}\{\gamma^2\} = \alpha^2 - \beta^2 \tag{9a}$$

$$\mathrm{Im}\{\gamma^2\} = 2\alpha\beta \tag{9b}$$

and combining these equations with (5) and (6), one obtains useful relations for the real and imaginary part of the relative permittivity

$$\varepsilon_r' = -\frac{\mathrm{Re}\{\gamma^2\}}{\omega^2\mu_0\varepsilon_0} \tag{10a}$$

$$\varepsilon_r'' = \frac{\mathrm{Im}\{\gamma^2\} - \omega\mu_0\sigma_c}{\omega^2\mu_0\varepsilon_0} \approx \frac{\mathrm{Im}\{\gamma^2\}}{\omega^2\mu_0\varepsilon_0} \tag{10b}$$

with $\sigma_c \approx 0$ for low-loss dielectric materials showing negligible conductivity.

In case of planar TLs and the previously discussed quasi-TEM propagation, the equations given earlier for a homogeneous material can be adapted using the effective permittivity method by simply replacing the relative permittivity ε_r by the effective relative permittivity $\varepsilon_{\mathrm{r,eff}}$ of the TL's cross section.

C. Combination of Propagation and TL Theory

The TL parameters can be written as

$$R' + j\omega L' = Z_c\gamma \qquad G' + j\omega C' = \frac{\gamma}{Z_c} \tag{11}$$

where R', L', G', and C' stand for the so-called RLGC parameters, namely, the series resistance, series inductance, shunt conductance, and shunt capacitance per unit length[3] and Z_c is the characteristic impedance of the TL.

Assuming a TL operating in a quasi-TEM mode of propagation, the propagation equation as shown before can be combined with TL theory as

$$\gamma = \sqrt{(R' + j\omega L')(G' + j\omega C')} \tag{12a}$$

$$= j\frac{\omega}{c_0}\sqrt{\mu_{\mathrm{r,eff}}\varepsilon_{\mathrm{r,eff}}} \tag{12b}$$

with $c_0 = (1/\sqrt{\mu_0\varepsilon_0})$ for the velocity of light in vacuum. Operating mostly in frequency ranges where the skin effect is well established, the associated redistribution of current inside the conductor increases the TL's series resistance. In addition, the series inductance is influenced as well, which can be modeled as [28]

$$L' = L'_{\mathrm{ext}} + L'_{\mathrm{int}} \approx L'_{\mathrm{ext}} + \frac{R'}{\omega} \tag{13}$$

which consists of the external inductance L'_{ext} as well as the contribution of the internal inductance L'_{int} per unit length and approaches the constant L'_{ext} for ideally smooth conductors at high frequencies, as L'_{int} vanishes with the increasing skin effect [28]. For rough conductors and skin depths in the order of magnitude of the surface roughness, the current flowing at the conductor surface cannot flow in a direct path anymore and needs to traverse the grooves introduced by the roughness, thus increasing the effective path length. As a consequence, not only the resistance and, thus, the loss increase by a substantial amount but also the inductance, since the grooves along the current path at the surface serve as distributed inductors [29], [30] (see Fig. 4). The characteristic impedance is then given as

$$Z_c = \sqrt{\frac{R' + j\omega(L'_{\mathrm{ext}} + L'_{\mathrm{int}})}{G' + j\omega C'}} = \sqrt{\frac{\mu}{\varepsilon}} = Z_0\sqrt{\frac{\mu_{\mathrm{r,eff}}}{\varepsilon_{\mathrm{r,eff}}}}. \tag{14}$$

The free-space impedance of the line with ideal conductors is given as [31]

$$Z_0 = \sqrt{\frac{\mu_0}{\varepsilon_0}} = \sqrt{\frac{L_0}{C_0}} = L_0c_0 = \frac{1}{C_0c_0} \tag{15}$$

where the dispersionless C_0 represents C' for the case that the TL is in free space (i.e., no dielectric substrate present) and $L_0 = L_{\mathrm{ext}}$ of the planar TL with ideal conductors ($\mu_r = 1$, $L_{\mathrm{int}} = 0$). Both L_0 and C_0 can easily be determined by full-wave simulations around dc using Ansys EM Suite or any available tool applying quasi-static approximations for impedance calculation of planar TLs.

As an interesting consequence to the equations given earlier, the following equations give an elegant way of describing the

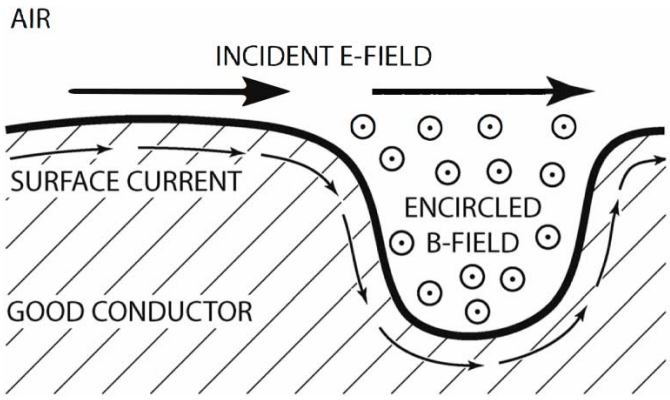

Fig. 4. From [29]. Magnetic field encircled by the surface current flowing on a rough conductor excited by the incident electric field results in substantial surface inductance, above and beyond that generated by the smooth surface skin effect.

[3]For the sake of convenience, the term "per unit length" speaking of the RLGC parameters is omitted in the following.

material parameters with respect to the RLGC parameters [31]

$$\mu_{\mathrm{r,eff}} = \frac{R' + j\omega L'}{j\omega L'_0} = \frac{R' + j\omega(L'_{\mathrm{ext}} + L'_{\mathrm{int}})}{j\omega L'_{\mathrm{ext}}} \tag{16a}$$

$$\varepsilon_{\mathrm{r,eff}} = \frac{G' + j\omega C'}{j\omega C'_0}. \tag{16b}$$

It should be mentioned that no equivalent concept to internal inductance exists for the shunt conductance, as long as the conductivity of the TL's conductor is sufficiently high and charge can be assumed to concentrate solely on the conductor's surfaces [28].

D. Characteristic Impedance and Inductance-Related Effects

Using the combined theory presented in the previous section, the characteristic impedance of the measured TL can be calculated. The propagation constant and effective permittivity $\varepsilon_{\mathrm{r,eff}}$ is already known from measurement with $\mu_{\mathrm{r,eff}} \approx 1$

$$\gamma = j\frac{\omega}{c_0}\sqrt{\mu_{\mathrm{r,eff}}\varepsilon_{\mathrm{r,eff}}} \approx j\frac{\omega}{c_0}\sqrt{\varepsilon_{\mathrm{r,eff}}}. \tag{17}$$

Following the same assumption, the characteristic impedance can be found as

$$Z_c = Z_0\sqrt{\frac{\mu_{\mathrm{r,eff}}}{\varepsilon_{\mathrm{r,eff}}}} \approx \frac{Z_0}{\sqrt{\varepsilon_{\mathrm{r,eff}}}} = \frac{L_0 c_0}{\sqrt{\varepsilon_{\mathrm{r,eff}}}} = \frac{1}{C_0 c_0\sqrt{\varepsilon_{\mathrm{r,eff}}}} \tag{18}$$

where C_0 or L_0 and, thus, Z_0 are found as described before. Knowing the propagation constant from measurement and the characteristic impedance from calculation, the RLGC parameters of the TL can be established as introduced in (11).

The increase in series resistance due to the skin depth as well as the roughness is already included in R' after measurement. However, the associated effect on phase is not accounted for in L', as $\mu_{\mathrm{r,eff}} \approx 1$ has been assumed in (17) and (18) for calculation of the RLGC parameters. Taking a look at (16a), it becomes obvious that for $\mu_{\mathrm{r,eff}} \approx 1$, $L'_{\mathrm{int}} = 0$ must follow. This models all the changes in phase originally related to L'_{int} and, thus, $\mu_{\mathrm{r,eff}}$ into the calculated $\varepsilon_{\mathrm{r,eff}}$ and, thus, C' instead of L', which effectively reduces the measured L' to $L' = L'_{ext}$ and increases C' above its correct value. Since L'_{int} and R' are related as shown in (13), the effective material parameters can be corrected as follows:

$$\mu_{\mathrm{r,eff,corr}} = \frac{R' + j\omega(L' + \frac{R'}{\omega})}{j\omega L'} \tag{19}$$

whereas (16a) is modified by substituting L'_{ext} with the measured L' and $L'_{\mathrm{int}} = \frac{R'}{\omega}$. Using (17), the effective relative permittivity can be corrected as [31]

$$\varepsilon_{\mathrm{r,eff,corr}} = -\frac{\gamma^2 c_0^2}{\mu_{\mathrm{r,eff,corr}}\omega^2} \tag{20}$$

which follows the propagation theory as given in (10a) to (10b) and allows for a correction of $\varepsilon_{\mathrm{r,eff}}$ by $\mu_{\mathrm{r,eff}}$ introduced through inductance-related effects (i.e., skin depth and surface roughness). An alternative formulation for the real part of the permittivity using the uncorrected effective permittivity known from the measurement and (16a) is given by

$$\varepsilon'_{\mathrm{r,eff,corr}} = \frac{\varepsilon'_{\mathrm{r,eff}}}{1 + \frac{L'_{\mathrm{int}}}{L'_{\mathrm{ext}}}}. \tag{21}$$

The corrected effective permittivity can be used to recalculate the characteristic impedance as given in (18) and ultimately to establish the corrected RLGC-parameters using (11).

E. Mapping of Effective Permittivity to Substrate Permittivity

The aforementioned theory allows the extraction of the effective permittivity of TLs the from measurements. For mapping this effective permittivity to the actual substrate permittivity, full-wave analysis is used. This ensures precision of the results compared to quasi-static models or predetermined fits as known from the literature, which are often subject to specific constraints on the TL geometry [32]. Even though the finite element solver by Ansys EM Suite is used in this paper, the authors want to point out that any full-wave solver can be used to perform the permittivity mapping.

For simulation, the cross section of the related TLs for each substrate is modeled in Ansys EM Suite, whereas the substrate permittivity is subject to a parameter sweep. The cross section of all TLs is obtained prior to the simulation as described in Section II-A, so that the layer buildup of every substrate is taken into account (especially in the case of CPW on SiO_2). The length of the simulated structure is chosen as 100 μm to keep meshing and thus computational effort low. The S-parameters obtained from simulation undergo the same processing as the measurement data as in the previous sections given earlier. The resulting effective permittivity is directly linked to the substrate permittivity known from the parameter sweep. Since the increase of effective permittivity with substrate permittivity for every frequency is linear over the whole simulated frequency range, the simulation results serve as the basis for a linear fit. The resulting fitting function (dependent on frequency and effective permittivity) can then be used to directly calculate the substrate permittivity for a given TL geometry simulated beforehand.

The portsize for simulation needs to be chosen sufficiently large to cover most of the simulated fields in the TL's cross section, so that the resulting S-parameters are converged and represent a real measurement. If the portsize is chosen too small, the effective permittivity extracted is not converged, and if the portsize is chosen too large, the computational effort increases and higher modes may occur, corrupting the simulation results or at least increasing the effort for evaluation of the results. An investigation of the correct portsize prior to the actual sweep assures convergence of the desired parameters.

F. Calculation of Total and Dielectric Loss

The total loss α of the TLs can directly be calculated from the measured propagation constant

$$\alpha = \mathrm{Re}(\gamma). \tag{22}$$

Considering the loss of the dielectric substrate material related to ε''_r, direct calculation is not feasible. Since the cross section of a planar TL consists of metallic (e.g., the MS conductor) as well as dielectric (e.g., air above and beside the conductor and substrate below the conductor) areas, the effective cross section shows a mixture of both loss effects. References [33] and [34] usually distinguish between

a good conductor [$(\sigma_{eq}/\omega\varepsilon') >> 1$] and a good dielectric [$(\sigma_{eq}/\omega\varepsilon') << 1$] here, assuming the material is homogeneous within its cross section. This approach cannot be applied to the effective cross section of a planar TL.

To be able to calculate ε'' using the general equation as given in (10b), we would have to extend the term σ_c to cover for some kind of effective conductivity of the cross section $\sigma_{\mathrm{c,eff}}$, which could be seen as an approach similar to the effective permittivity method. This task is very ambitious and requires the development of a new theory as well as extensive modifications of the available simulation tools. Moreover, as the existing models for separation of conductor and dielectric loss do not cover the influence of surface roughness sufficiently well [29] and are mostly only applicable for MS and not planar TL in general [32], the authors decided to favor an approach using a general formulation.

The Kramers–Kronig relations [35]

$$\varepsilon'_{\mathrm{r}}(\omega)-1=\frac{1}{\pi}\int_{-\infty}^{\infty}\frac{\varepsilon''_{\mathrm{r}}(\omega')}{\omega'-\omega}d\omega'=\frac{2}{\pi}\int_{0}^{\infty}\frac{\omega'\varepsilon''_{\mathrm{r}}(\omega')}{\omega'^2-\omega^2}d\omega' \quad (23a)$$

$$\varepsilon''_{\mathrm{r}}(\omega)=\frac{1}{\pi}\int_{-\infty}^{\infty}\frac{\varepsilon'_{\mathrm{r}}(\omega')}{\omega'-\omega}d\omega'=\frac{2}{\pi}\int_{0}^{\infty}\frac{\omega\varepsilon'_{\mathrm{r}}(\omega')}{\omega'^2-\omega^2}d\omega' \quad (23b)$$

connect the real and imaginary parts of a complex function such as the permittivity as shown here, while ensuring causality of the considered complex parameter (see [35] for further reading on permittivity theory). As a consequence, these equations imply

$$\varepsilon'_{\mathrm{r}} \propto \varepsilon''_{\mathrm{r}} \quad (24)$$

so that the imaginary part of the permittivity can be calculated if the real part is already known and vice versa. Using the multipole Debye formulation as suggested in [36]

$$\varepsilon_{\mathrm{r}}(\omega)=\varepsilon_{\infty}+(\varepsilon_{\mathrm{dc}}-\varepsilon_{\infty})\sum_{n=1}^{N}\frac{g_n}{1+j\omega\tau_n} \quad (25)$$

with $\varepsilon_{\mathrm{dc}}$ as the static limit, ε_{∞} as the infinite frequency limit, $\tau_n=(1/\omega_r)=(1/2\pi f_r)$ as the inverse of the angular relaxation frequency f_r, N as the order of the generalized Debye model and g_n as the weight at the corresponding relaxation frequency, the real and imaginary parts of the permittivity can be separated

$$\varepsilon'_{\mathrm{r}}(\omega)=\varepsilon_{\infty}+(\varepsilon_{\mathrm{dc}}-\varepsilon_{\infty})\sum_{n=1}^{N}\frac{g_n}{1+(\omega\tau_n)^2} \quad (26a)$$

$$\varepsilon''_{\mathrm{r}}(\omega)=(\varepsilon_{\mathrm{dc}}-\varepsilon_{\infty})\sum_{n=1}^{N}\frac{\omega\tau_n g_n}{1+(\omega\tau_n)^2}. \quad (26b)$$

Solutions to the given set of equations should follow the constraints [36]

$$\sum_{n=1}^{N}g_n=1, \quad g_n>0, \ \varepsilon_{\mathrm{dc}}\geq\varepsilon_{\infty}\geq 1. \quad (27)$$

With the equations given earlier, the imaginary part of the substrate permittivity can be calculated from the given real part.

1) The already determined real part of the substrate permittivity is fit to the model given in (26a). For this fit, a pattern search optimization procedure using MATLAB R2016a is applied. The optimization intervals as well as the starting values for the static and infinite frequency limits can easily be estimated from the measurement data. The weights g_n are allowed to a value of]0, 1[, thus enforcing multiple poles. The relaxation frequencies f_r are assumed in the megahertz to gigahertz range [37]. N is chosen to 3, since this already is sufficient for convergence of the fit for the measurements shown in this paper.
2) The parameters obtained by the fit are used for calculation of the imaginary part using (26b).
3) The real and imaginary parts can be combined into the dielectric loss tangent $\tan\delta_d$ as stated in (7).

The authors want to point out that due to the interval bounds given in (23a) and(23b), the equations derived earlier only hold true if the whole (infinite) spectrum of either the real or imaginary part of the permittivity is known. Even though this cannot be satisfied in reality, it is assumed that the given theory can be applied due to the broad measurement bandwidth used in this paper.

Assuming a broad enough measurement bandwidth as well as quality of the fit applied for the real and imaginary parts of the permittivity, the models given could ultimately be used to extrapolate the measured data from the minimum measurement frequency (such as 500 MHz in this paper) downward to dc or even to frequencies above the maximum measurement frequency. This approach is to be treated with caution, however, since there are several constraints to be considered for extension in both directions of frequency, such as physical phenomena with influence on the dielectric behavior of a material not covered by the initial model given in (25) (i.e., the Maxwell–Wagner effect near dc [38] or dielectric resonances such as ionic and electronic polarization, which usually first take place in the range of a few terahertz [37]). The authors refer to [36]–[38] for further reference and suggest the implementation of a more advanced model in the future (i.e., for frequencies approaching the terahertz range), if necessary. Besides this remark concerning extrapolation, the given model should safely allow an interpolation of the measurement data, such as in the frequency gap from 67–140 GHz in this paper.

To evaluate the quality of fit in comparison to the measurement data, the mean absolute error

$$\mathrm{MAE}=\frac{1}{n}\sum_{i=1}^{n}|m_i-f_i| \quad (28)$$

is used, with m_i and f_i denoting the measurement and fit data at a certain frequency point, respectively, while n stands for the number of frequency points.

IV. Measurement Results and Discussion

The given theory is used to extract the effective substrate permittivity from measurement and map the measured data to the physical substrate permittivity using simulations, with the results for the different materials measured shown in Figs. 5–11. In addition, a fit of the measurement data

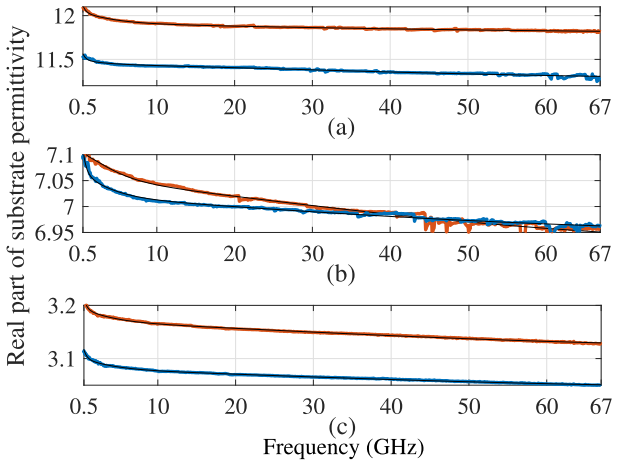

Fig. 5. Measured real part of substrate permittivity for (a) RO3010, (b) RO3006, and (c) RO3850 substrates. Blue and red lines indicate data for MS and GCPW, respectively, while the obtained fit is shown in black. Reference values for 10 GHz as given by the substrate manufacturer are 3.14 for RO3850, 6.50 for RO3006, and 11.20 for RO3010.

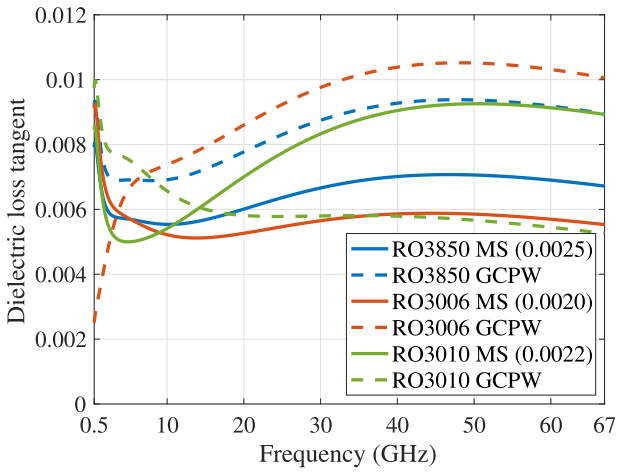

Fig. 6. Dielectric loss tangent obtained from the fitted measurement data for different PCB materials. Reference values for 10 GHz as given by the substrate manufacturer are given in brackets and apply for MS and GCPW.

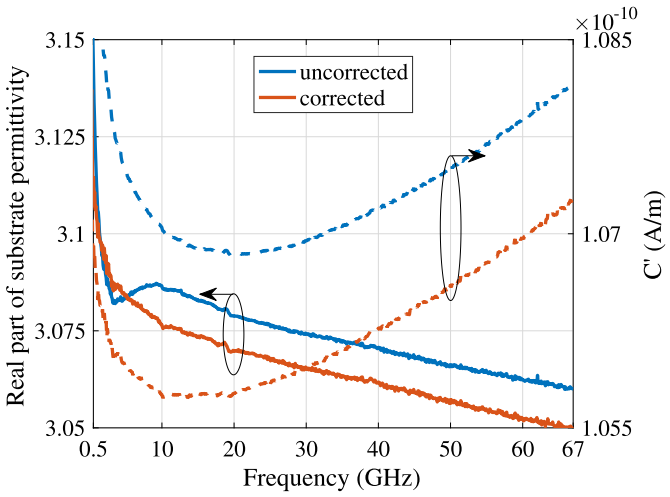

Fig. 7. Measured real part of the substrate permittivity (solid lines) and shunt capacitance (dashed lines) before and after correction for inductance-related effects for RO3850.

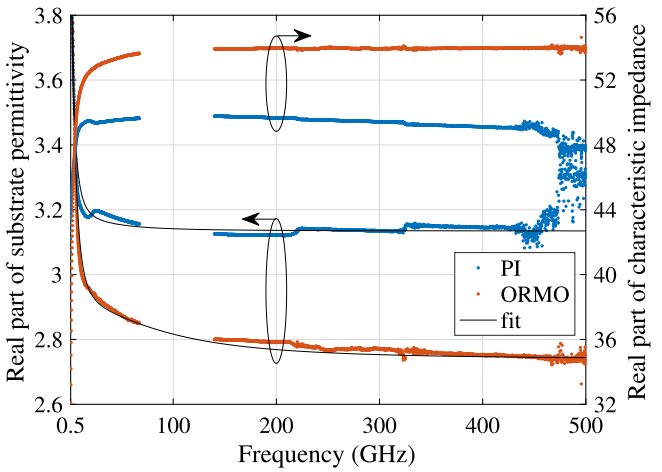

Fig. 8. Measured real part of the substrate permittivity (left) and characteristic impedance (right) for PI and ORMO. Black solid lines: fit on substrate permittivity data.

to the model used for extraction of the dielectric loss tangent as shown in (26a) is given (including interpolated data for 67–140 GHz in case of the on-chip substrates). In Sections IV-A and IV-B, the results for both PCB and on-chip substrates will be discussed and compared to reference data.

A. PCB Substrates

For the three PCB substrates, the substrate manufacturer gives measurement values for the substrate permittivity as well as loss tangent at 10 GHz in the respective datasheets, which represent the average values found by the measurements of several lots of substrates of different substrate heights. Comparing this averaged reference data with the measurements shown in Fig. 5, the given values agree with the measurement results for MS within a deviation of about 0.1 (3%) for RO3850, about 0.5 (8%) for RO3006, and about 0.3 (3%) for RO3010. The GCPW values show about identical dispersion and a small offset in magnitude, which can be explained by a small anisotropy of the substrate and the different directions of characterization due to the minimal different orientations of the electrical field lines in MS and GCPW. The fits for all measurements on PCB agree within a mean absolute error in the order of magnitude of 0.001. Concerning the determined loss tangent shown in Fig. 6, the values are in the same order of magnitude, but two to three times higher than the loss tangent given in the data sheets of the substrates.

In Fig. 7, the values before and after correction for inductance-related effects for the substrate permittivity and shunt capacitance of the measured MS on UL3850 are given. For the substrate permittivity prior to correction, a decrease at about 7.5 GHz can be observed in the slope. It is only after correction that the values comply with general permittivity theory, which suggests a continuous slope and decrease of the values from dc onward, while the magnitude as well as dispersion of the slope are dependent on the material [37], [38].

The deviations of the measurement data from the averaged reference data for the three given values of permittivity covering a range from about 3 to about 12 are within a

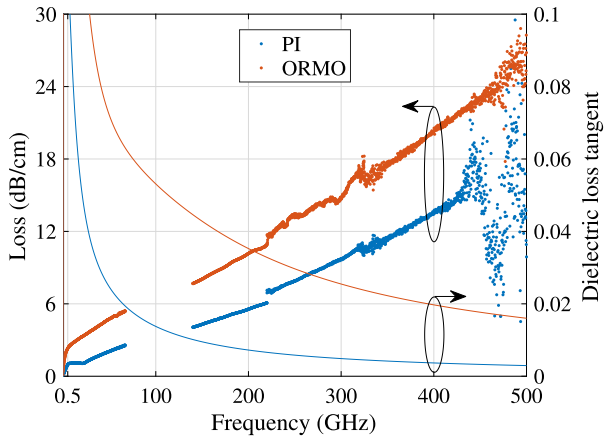

Fig. 9. Measured total loss (left) and dielectric loss tangent obtained from fit measurement data (right) for PI and ORMO.

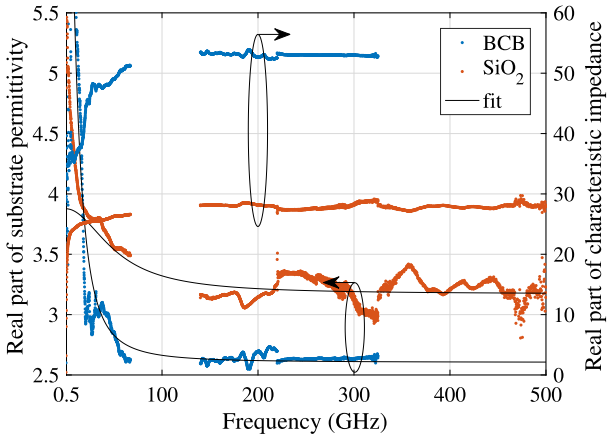

Fig. 10. Measured real part of the substrate permittivity (left) and characteristic impedance (right) for BCB and SiO_2. Black solid lines: fit on substrate permittivity data.

single-digit percentage. Although the actual uncertainty of the presented method will be addressed by the authors in future publications, this already gives an implicit measure of the precision of the method over a broad range of permittivity values. The loss tangent results deviate by a small factor, while the order of magnitude agrees with the reference data, which is usually sufficient for most applications. Even though careful analysis of the aforementioned deviations needs to be addressed in future publications, the authors deem this preliminary evaluation as sufficient to emphasize the feasibility of the presented method.

B. On-Chip Substrates

1) PI and ORMO: The ORMO substrate can be measured up to 500 GHz, while the data for the PI substrate is not suitable for frequencies above about 440 GHz. The measurement data at the end of the measurement frequency range shows significant noise, but falling below the dynamic range of the measurement gives no explanation for the cutoff frequency of 440 GHz, since it can be observed in the raw measurement data even for the shortest calibration line already. The authors assume that the probe pad is supporting higher modes of propagation or even radiation due to its planar dimensions.

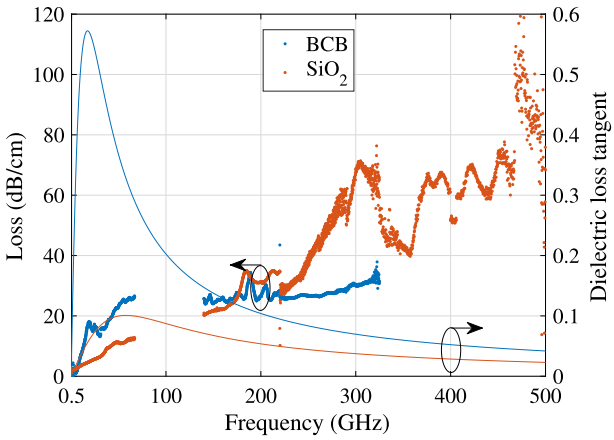

Fig. 11. Measured total loss (left) and dielectric loss tangent obtained from fit measurement data (right) for BCB and SiO_2.

At a frequency of 440 GHz, the effective wavelength is about 435 μm, which is roughly the distance in-between the vias at each side of the probe pad and, thus, can show a resonance. This is backed by similar observations done by Seiler *et al.* [27].

Besides this remark, the fits for the permittivity data agree within a mean absolute error of 0.020 and 0.011 for PI and ORMO, respectively. Apart from the range of convergence from 0.5 to 67 GHz, the PI substrate shows a permittivity of about 3.15 over the whole frequency range, which remains almost constant for the higher frequencies. In comparison, the ORMO substrate shows a small dispersion in the permittivity from about 2.8 at 140 GHz to about 2.7 at 500 GHz. The total loss for the ORMO substrate is three to four times higher (about 4 to 6 dB/cm) as for the PI substrate, which is reflected in the loss tangent accordingly.

In general, it is expected that the on-chip substrates show increased total loss compared to the PCB substrates. As the on-chip substrates are of very low height to enable operation in the subterahertz-range (e.g., suppress higher order modes, see [23]), the planar conductor dimensions need to get smaller to comply with a 50-Ω measurement environment. As a consequence, the effective conductor width available for conduction purposes reduces, and thus, the resistivity per unit length of TLs fabricated on such substrates increases accordingly. Since the skin effect is very well established in the subterahertz-range and for the given conductor dimensions, mainly the conductor width contributes to this effect in case of MS. For (G)CPW, the main current density is given on the conducting surfaces in-between the signal and ground conductor, which is why the conductor thickness is more of relevance here.

2) BCB and SiO_2: Due to the constraints of the custom BCB process and a resulting larger probe pad size, the BCB substrate can only be measured up to 325 GHz.

Considering the BCB and SiO_2 substrates in general, the measurement data are not as smooth compared to the PI and ORMO measurements. The authors explain this as follows: for the fabrication of the BCB substrate, a recently developed custom process is used, which shows a variation of the thickness of the top metallization across the overall substrate. This has an influence on the quality of the probe-pad

interface (e.g., contact resistance), which affects the phase and loss measurement and reduces the repeatability of measurements. In addition, the yield of the fabricated structures for calibration and measurement was not very high. As a result, several contacting attempts on calibration and measurement structures distributed on the overall substrate are necessary during calibration and measurement, which emphasizes this issue even more.

In case of the SiO_2 substrate, only a limited amount of chips is available for measurement, which basically imposes the same problem as for the BCB substrate. In addition, the top metal here is aluminum, which is rather soft and tends to roughen during multiple connections with a probe, which is why contact quality and repeatability are affected even further.

As a consequence, the measurement data, as well as the obtained fit, are not of comparable quality as for the PI and ORMO substrates. The mean absolute error for the fit on the BCB data is 0.127, while for the fit on the SiO_2 data, it is 0.076. Nevertheless, a general trend for both substrates can be deduced, with BCB showing a permittivity of about 2.6 and SiO_2 of about 3.3 for the higher frequencies. The BCB substrate shows a higher loss than the SiO_2 substrate, while both substrates perform worse compared to the PI and ORMO substrates, as the total loss is significantly higher. The authors want to point out that the total loss and loss tangent derived for BCB and SiO_2 are to be interpreted with caution, as the aforementioned issues concerning the measurement can have an influence on the data.

3) Comparison to Reference Data: The authors want to point out that a comparison of the measurement data presented in this paper with reference data provided by other authors proves to be difficult since only a very small number of publications addressing material characterization techniques and measurements of comparable materials at the given frequencies exists yet.

For thin-film substrates at these frequencies, Williams *et al.* [22] presented a terahertz BCB substrate as a suitable substrate material for subterahertz applications in comparison with a silicon-on-insulator substrate. While the mentioned paper gives no values for substrate permittivity and dielectric loss, the shown data for the effective permittivity and total loss can be compared to the measured data given in this paper. However, it should be noted that the MS TLs used on the substrates given there differ in their cross-sectional dimensions and, thus, expected conductor loss (assuming comparable metal conductivity), which renders an inference to dielectric loss infeasible. From [22, Fig. 9], the same roughness in the data as for BCB and SiO_2 can be seen, which indicates similar issues as already discussed earlier are present in this measurement as well. This underlines the difficulty of measurements of planar substrates at those frequencies in general.

Both the PI and ORMO substrates show similar performance as the terahertz BCB substrate presented in [22]. The shown data for the effective permittivity and total loss is comparable to the measured data for PI and ORMO and, thus, implies comparable low-k characteristics (i.e., low dispersion and loss). Comparing the total loss at 200 GHz, the terahertz BCB indicates a value of about 10 dB/cm, while PI and ORMO show values of 5.6 and 10.2 dB/cm, respectively, with the PI substrate outperforming the terahertz BCB by almost a factor of 3 (about 4.4 dB/cm). Therefore, both the PI and ORMO substrates can be considered suitable for subterahertz applications.

For the PI substrate, Ponchak and Downey [39] give values for the effective permittivity and total loss of MS TLs on thin-film PI substrates up to 110 GHz. Comparing the reference MS line of about 50 Ω given there ($w = 21.7\ \mu$m and $h = 7.4\ \mu$m in [39]) with the results obtained for the 50-Ω MS line measured in this paper, the reference MS shows an effective permittivity of about 2.5 and a total loss of about 4 dB/cm, while the MS line measured in this paper shows an effective permittivity of 2.45 and a total loss of 2.36 dB/cm.

No reference measurements for the ORMO substrate could be found by the authors.

For the BCB substrate, direct comparison to the terahertz BCB given in [22] is applicable: The terahertz BCB shows an effective permittivity of about 2.25 and a total loss of about 10 dB/cm at 200 GHz. The BCB substrate measured in this paper shows an effective permittivity of about 2.15 and a total loss of about 25 dB/cm. The significantly higher loss measured in this paper is attributed to the aforementioned issues during measurement.

Comparison of the effective permittivity and total loss of the measured CPW on the SiO_2 substrate to the MS on a silicon-on-insulator substrate given in [22] is not feasible.

V. Conclusion

Measurement data of three PCB substrate materials up to 67 GHz is used to evaluate the presented method and shows agreement within a single-digit percentage with reference data given by the substrate manufacturer. The feasibility of the given method for frequencies in the subterahertz range is shown by characterizing promising material candidates for applications up to 500 GHz. The PI and ORMO substrates perform well in comparison to reference data, while the PI substrate outperforms a specially designed subterahertz BCB substrate known from the literature as well as reference data on PI up to 110 GHz. The BCB and SiO_2 could be characterized in terms of permittivity and characteristic impedance as well, but show significantly worse performance in terms of loss, which is attributed to issues during fabrication and measurement.

References

[1] M. Jenning *et al.*, "Energy-efficient transceivers for ultra-highspeed computer board-to-board communication," in *Proc. IEEE Int. Conf. Ubiquitous Wireless Broadband*, Oct. 2015, pp. 1–5.

[2] Y. Kobayashi and M. Katoh, "Microwave measurement of dielectric properties of low-loss materials by the dielectric rod resonator method," *IEEE Trans. Microw. Theory Techn.*, vol. MTT-33, no. 7, pp. 586–592, Jul. 1985.

[3] L. Chen, C. K. Ong, and B. T. G. Tan, "Amendment of cavity perturbation method for permittivity measurement of extremely low-loss dielectrics," *IEEE Trans. Instrum. Meas.*, vol. 48, no. 6, pp. 1031–1037, Dec. 1999.

[4] J. Krupka, W. Gwarek, N. Kwietniewski, and J. G. Hartnett, "Measurements of planar metal–dielectric structures using split-post dielectric resonators," *IEEE Trans. Microw. Theory Techn.*, vol. 58, no. 12, pp. 3511–3518, Dec. 2010.

[5] H. B. Wang and Y. J. Cheng, "Broadband printed-circuit-board characterization using multimode substrate-integrated-waveguide resonator," *IEEE Trans. Microw. Theory Techn.*, vol. 65, no. 6, pp. 2145–2152, Jun. 2017.
[6] A. Kik, "Complex permittivity measurement using a ridged waveguide cavity and the perturbation method," *IEEE Trans. Microw. Theory Techn.*, vol. 64, no. 11, pp. 3878–3886, Nov. 2016.
[7] S. B. Cohn and K. C. Kelly, "Microwave measurement of high-dielectric-constant materials," *IEEE Trans. Microw. Theory Techn.*, vol. MTT-14, no. 9, pp. 406–410, Sep. 1966.
[8] W. E. Courtney, "Analysis and evaluation of a method of measuring the complex permittivity and permeability microwave insulators," *IEEE Trans. Microw. Theory Techn.*, vol. MTT-18, no. 8, pp. 476–485, Aug. 1970.
[9] Y. F. Gui, W. B. Dou, P. G. Su, and K. Yin, "Improvement of open resonator technique for dielectric measurement at millimetre wavelengths," *IET Microw., Antennas Propag.*, vol. 3, no. 7, pp. 1036–1043, Oct. 2009.
[10] W.-B. Dou and B. Xiang, "A new open cavity at millimeter wave band for permittivity measurement of dielectrics," *Prog. Electromagn. Res. M*, vol. 29, pp. 181–192, Feb. 2013.
[11] A. M. Nicolson and G. F. Ross, "Measurement of the intrinsic properties of materials by time-domain techniques," *IEEE Trans. Instrum. Meas.*, vol. IM-19, no. 4, pp. 377–382, Nov. 1970.
[12] W. B. Weir, "Automatic measurement of complex dielectric constant and permeability at microwave frequencies," *Proc. IEEE*, vol. 62, no. 1, pp. 33–36, Jan. 1974.
[13] J. Baker-Jarvis, M. D. Janezic, J. H. Grosvenor, Jr., and R. G. Geyer, "Transmission/reflection and short-circuit line methods for measuring permittivity and permeability," Dept. Commerce, Nat. Inst. Standards Technol. (NIST), Gaithersburg, MD, USA, Tech. Rep. 1355-R, 1993.
[14] M. W. Hyde, IV, M. J. Havrilla, and A. E. Bogle, "Nondestructive determination of the permittivity tensor of a uniaxial material using a two-port clamped coaxial probe," *IEEE Trans. Microw. Theory Techn.*, vol. 64, no. 1, pp. 239–246, Jan. 2016.
[15] S. I. Shams, M. M. Tahseen, and A. A. Kishk, "Wideband relative permittivity characterization of thin low permittivity textile materials based on ridge gap waveguides," *IEEE Trans. Microw. Theory Techn.*, vol. 64, no. 11, pp. 3839–3850, Nov. 2016.
[16] J. Tang *et al.*, "Characterization of y-bias ferrite materials for tunable antenna applications using a partially filled rectangular waveguide," *IEEE Trans. Antennas Propag.*, vol. 65, no. 10, pp. 5279–5288, Oct. 2017.
[17] C.-Y. Ho, H.-H. Cheng, P.-C. Pan, C.-C. Wang, and C.-P. Hung, "Dielectric characterization of ultra-thin low-loss build-up substrate for system-in-package (SiP) modules," *IEEE Trans. Microw. Theory Techn.*, vol. 63, no. 9, pp. 2923–2930, Sep. 2015.
[18] J. Baker-Jarvis, E. J. Vanzura, and W. A. Kissick, "Improved technique for determining complex permittivity with the transmission/reflection method," *IEEE Trans. Microw. Theory Techn.*, vol. 38, no. 8, pp. 1096–1103, Aug. 1990.
[19] W. Barry, "A broad-band, automated, stripline technique for the simultaneous measurement of complex permittivity and permeability," *IEEE Trans. Microw. Theory Techn.*, vol. MTT-34, no. 1, pp. 80–84, Jan. 1986.
[20] A. Deutsch, G. Arjavalingam, G. V. Kopcsay, and M. J. Degerstrom, "Short-pulse propagation technique for characterizing resistive package interconnections," *IEEE Trans. Compon., Hybrids, Manuf. Technol.*, vol. 15, no. 6, pp. 1034–1037, Dec. 1992.
[21] A. Deutsch *et al.*, "Application of the short-pulse propagation technique for broadband characterization of pcb and other interconnect technologies," *IEEE Trans. Electromagn. Compat.*, vol. 52, no. 2, pp. 266–287, May 2010.
[22] D. F. Williams *et al.*, "Calibration-kit design for millimeter-wave silicon integrated circuits," *IEEE Trans. Microw. Theory Techn.*, vol. 61, no. 7, pp. 2685–2694, Jul. 2013.
[23] P. Seiler, B. Klein, and D. Plettemeier, "Analytical and experimental investigation of substrate permittivity and loss up to 67 GHz," in *Proc. 20th Asia-Pacific Conf. Commun. (APCC)*, Oct. 2014, pp. 123–128.
[24] P. Seiler and D. Plettemeier, "Permittivity and loss characterization of thin-film substrates up to 220 GHz," in *Proc. IEEE Int. Symp. Antennas Propag. USNC/URSI Nat. Radio Sci. Meeting (APS/URSI)*, Jul. 2017, pp. 891–892.
[25] P. Seiler, B. Klein, and D. Plettemeier, "Internal inductance correction for permittivity measurements of planar transmission lines," in *Proc. Int. Symp. Antennas Propag. (ISAP)*, Oct. 2016, pp. 732–733.
[26] R. B. Marks, "A multiline method of network analyzer calibration," *IEEE Trans. Microw. Theory Techn.*, vol. 39, no. 7, pp. 1205–1215, Jul. 1991.
[27] P. Seiler, B. Klein, and D. Plettemeier, "Influence of microstrip probe pad design on planar measurements using on-wafer probes," in *Proc. Int. Symp. Antennas Propag. (ISAP)*, Nov. 2015, pp. 1–4.
[28] H. Johnson and M. Graham, *High Speed Signal Propagation: Advanced Black Magic*. Upper Saddle River, NJ, USA: Prentice-Hall, 2003.
[29] A. F. Horn, J. W. Reynolds, and J. C. Rautio, "Conductor profile effects on the propagation constant of microstrip transmission lines," in *IEEE MTT-S Int. Microw. Symp. Dig.*, May 2010, pp. 868–871.
[30] Y. Shlepnev and S. McMorrow, "Nickel characterization for interconnect analysis," in *Proc. IEEE Int. Symp. Electromagn. Compat.*, Aug. 2011, pp. 524–529.
[31] R. B. Marks, D. F. Williams, and M. B. Steer, "Accurate experimental characterization of interconnects: A discussion of 'Experimental electrical characterization of interconnects and discontinuities in high-speed digital systems,"' *IEEE Trans. Compon., Hybrids, Manuf. Technol.*, vol. 15, no. 4, pp. 601–604, Aug. 1992.
[32] M. Kirschning and R. H. Jansen, "Accurate model for effective dielectric constant of microstrip with validity up to millimetre-wave frequencies," *Electron. Lett.*, vol. 18, no. 6, pp. 272–273, Mar. 1982.
[33] C. A. Balanis, *Advanced Engineering Electromagnetics*. Hoboken, NJ, USA: Wiley, 2002.
[34] J. D. Jackson, *Classical Electrodynamics*. Hoboken, NJ, USA: Wiley, 1998.
[35] C. J. F. Bottcher, *Theory of Electric Polarization, Dielectrics in Time-Dependent Fields*, vol. 2. Amsterdam, The Netherlands: Elsevier, 1978.
[36] B. Oswald, J. Doetsch, and K. Roth, "A new computational technique for processing transmission-line measurements to determine dispersive dielectric properties," *Geophysics*, vol. 71, no. 2, pp. K31–K35, Mar./Apr. 2006.
[37] S. Ramo, J. R. Whinnery, and T. Van Duzer, *Fields and Waves in Communication Electronics*. Hoboken, NJ, USA: Wiley, 1994.
[38] A. K. Jonscher, "Dielectric relaxation in solids," *J. Phys. D, Appl. Phys.*, vol. 32, pp. R57–R70, Jul. 1999.
[39] G. E. Ponchak and A. N. Downey, "Characterization of thin film microstrip lines on polyimide," *IEEE Trans. Compon., Packag., Manuf. Technol. B, Adv. Packag.*, vol. 21, no. 2, pp. 171–176, May 1998.

Patrick Seiler (GS'14) received the B.Sc. and M.Sc. degrees (Hons.) in electrical engineering from the Technische Universität Berlin, Berlin, Germany, in 2011 and 2012, respectively. He is currently pursuing the Ph.D. degree in electrical engineering at the Chair for Radio Frequency and Photonics Engineering, Technische Universität Dresden, Dresden, Germany.

Since 2013, he has been a Research Associate with the Chair for Radio Frequency and Photonics Engineering, Technische Universität Dresden. He is currently with the Center for Advancing Electronics Dresden and the Collaborative Research Center, Highly Adaptive Energy-Efficient Computing, where he is involved in electronics and energy-efficient computing systems for future applications. His current research interests include calibration and on-wafer measurement techniques up to terahertz frequencies with a focus on material characterization, as well as electromagnetic wave propagation and transmission line modeling.

Dirk Plettemeier (S'95–M'04) received the Ph.D. degree in electrical engineering from Ruhr-Universität Bochum, Bochum, Germany.

Since 2011, he has been a Full Professor with the Chair for Radio Frequency and Photonics Engineering, Technische Universität Dresden, Dresden, Germany. He has been involved in several international scientific activities as a Co-Investigator for ESA and NASA space missions such as Cassini-Huygens, Rosetta and ExoMars, mainly focusing on subsurface imaging. He is currently with the Center for Advancing Electronics Dresden and the Collaborative Research Center, Highly Adaptive Energy-Efficient Computing, where he is involved in electronics and energy-efficient computing systems for future applications. His current research interests include millimeter-wave and terahertz systems with a focus on antennas and chip-integrated applications, wave propagation, and remote sensing, as well as imaging solutions for space applications.